PAPER

Check for updates

Facile preparation of 3D porous agar-based heteroatom-doped carbon aerogels for high-energy density supercapacitors†

Kaijun Xie,‡ Kai Xia,‡ Xin Ding, ID * Long Fang, Xin Liu and Xiaodong Zhang ID *

The fabrication of heteroatom-doped porous carbon materials with high electrical conductivity and large specific surface area *via* an environmentally friendly route is critical and challenging. Herein, nitrogen and oxygen co-doped agar porous carbon (APC) was developed for supercapacitors *via* a one-step carbonization method with agar as the raw material and ammonia as the activator and nitrogen source. APC outperformed pectin porous carbon, tamarind porous carbon, and the previously reported carbon-based supercapacitors with a high capacitance retention of 72% even from 0.5 A g^{-1} to 20 A g^{-1} and excellent cycling stability in 6 M KOH solution (retained after 10 000 cycles) with a rate of over 98.5%. Furthermore, the APC electrode-based symmetric device exhibited an impressive energy density of 20.4 W h kg^{-1} and an ultra-high power density of 449 W kg^{-1} in 1 M Na$_2$SO$_4$ electrolyte together with excellent cycling stability (103.2% primary capacitance retentivity after 10 000 cycles). This study offers a novel method for the synthesis of nitrogen heteroatom-doped hierarchical porous carbon materials for performance-enhanced energy storage devices.

1. Introduction

The excessive utilization of fossil fuels has greatly promoted rapid industrial development, while also causing environmental pollution, ecological damage, and greenhouse effect, which seriously threaten human survival and development.[1,2] New alternative energy sources, such as solar energy, wind energy, tidal energy, hydrogen energy, and geothermal energy, have been developed and attract great attention.[3–5] However, due to natural conditions, these intermittent energies cannot supply a stable and continuous energy supply.[6] Thus, to solve the inherent discontinuity issue, supercapacitors, featuring fast charge and discharge, high power density, long cycle life, stable rate performance, excellent low-temperature performance, and environmental friendliness, are considered perfect candidates.[7–9]

Supercapacitors use reversible electrosorption to store the electrical energy of charged species at the carbon–electrolyte interface, enabling fast energy harvesting/transfer within seconds and potential operating lifetimes surpassing one million cycles.[10–13] To achieve high energy density, porous electrodes with a large specific surface area are required.[14] Particularly, microporous carbons with pores smaller than

College of Chemistry and Chemical Engineering, Qingdao University, Qingdao 266071, China. E-mail: dingxin@qdu.edu.cn; zhangxdqd@hotmail.com

† Electronic supplementary information (ESI) available. See https://doi.org/10.1039/d2ra03685a

‡ These authors contributed equally to this work.

2 nm have demonstrated exceptional capacitive energy storage capabilities.[15–18] In recent years, coal, pitch, polysaccharides, carbon aerogels, *etc.* have been studied as potential electrode materials. Among them, polysaccharides can be obtained from a wide range of sources at low prices, showing tremendous practical applications.[19–21] Their phase and pores can be adjusted by tuning temperature and concentration, and activators can also be employed to change the type of pores to obtain optimized electrical properties.[19–28] Generally, KOH, ZnCl$_2$, and CaCl$_2$ are used as activators to obtain larger specific surface area;[29] however, they also result in unavoidable equipment corrosion and environmental pollution. Additionally, due to their high oxygen content and poor electrochemical performance,[30] the energy storage performance of supercapacitors is usually poor.[30,31] Therefore, an effective and environmentally friendly pathway is necessary to change their structures.[32,33] Ammonia treatment technology accomplishes this goal in one step, where nitrogen creates abundant pores to achieve larger specific surface area and replace partial oxygen atoms in agar for higher electrical conductivity.[34] Additionally, oxygen and nitrogen functional groups not only improve wettability, but also provide additional false capacitance during the charge and discharge process.[35]
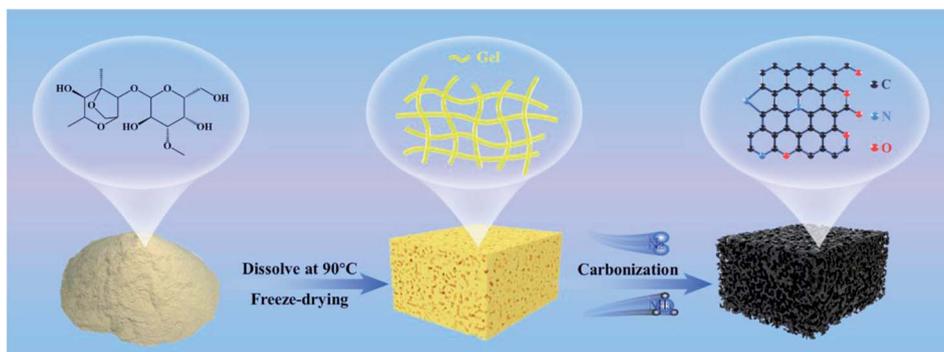
Herein, an agar porous carbon (APC) aerogel was prepared *via* freeze-drying and then high-temperature carbonization pathway as shown in Scheme 1. Moreover, pectin porous carbon (PPC) aerogel and tamarind porous carbon (TPC) aerogels were also synthesized using the same approach.[35–37] A layered porous

Scheme 1 Schematic of the preparation of the symmetric supercapacitor.

structure conducive to ion/electron transport and charge storage was obtained, resulting in a higher specific capacitance, rate performance and cycle stability. An ultra-high specific capacity of 272 F g^{-1} at a current density of 0.5 A g^{-1} was obtained. Moreover, even in 6 M KOH electrolyte, at the current density of 10 A g^{-1}, a capacity of 210 F g^{-1} was retained, which is superior to that of PPC, TPC and nearly all reported carbon-based supercapacitors. The capacity retention rate after 10 000 cycles was as high as 98.5%. In addition, symmetrical APC//APC supercapacitors showed a wide voltage window of 1.8 V, high
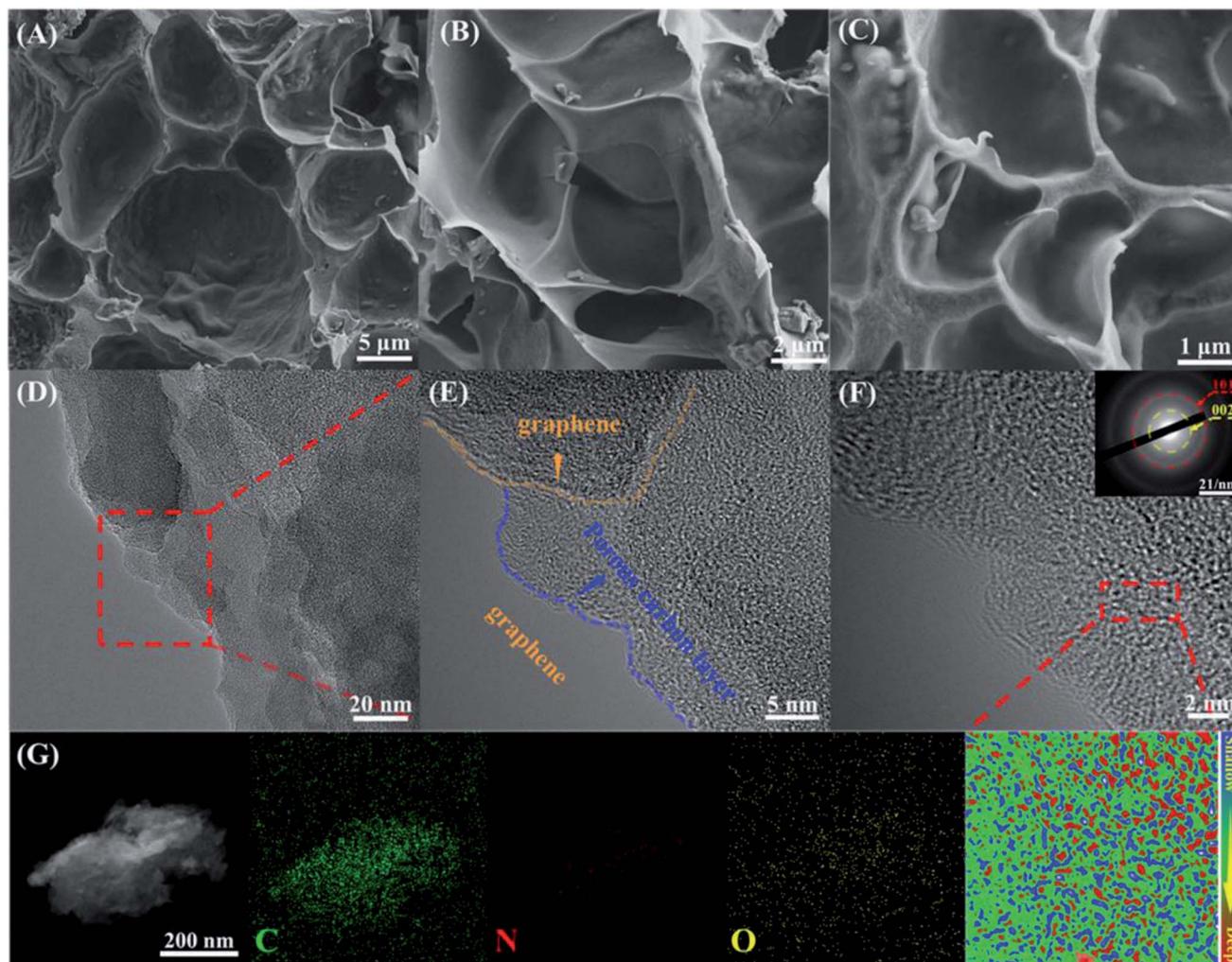

Fig. 1 (A)–(C) SEM images of APC. (D)–(F) HR-TEM images of APC. (G) EDS elemental mapping images of C, N, and O in APC, respectively.
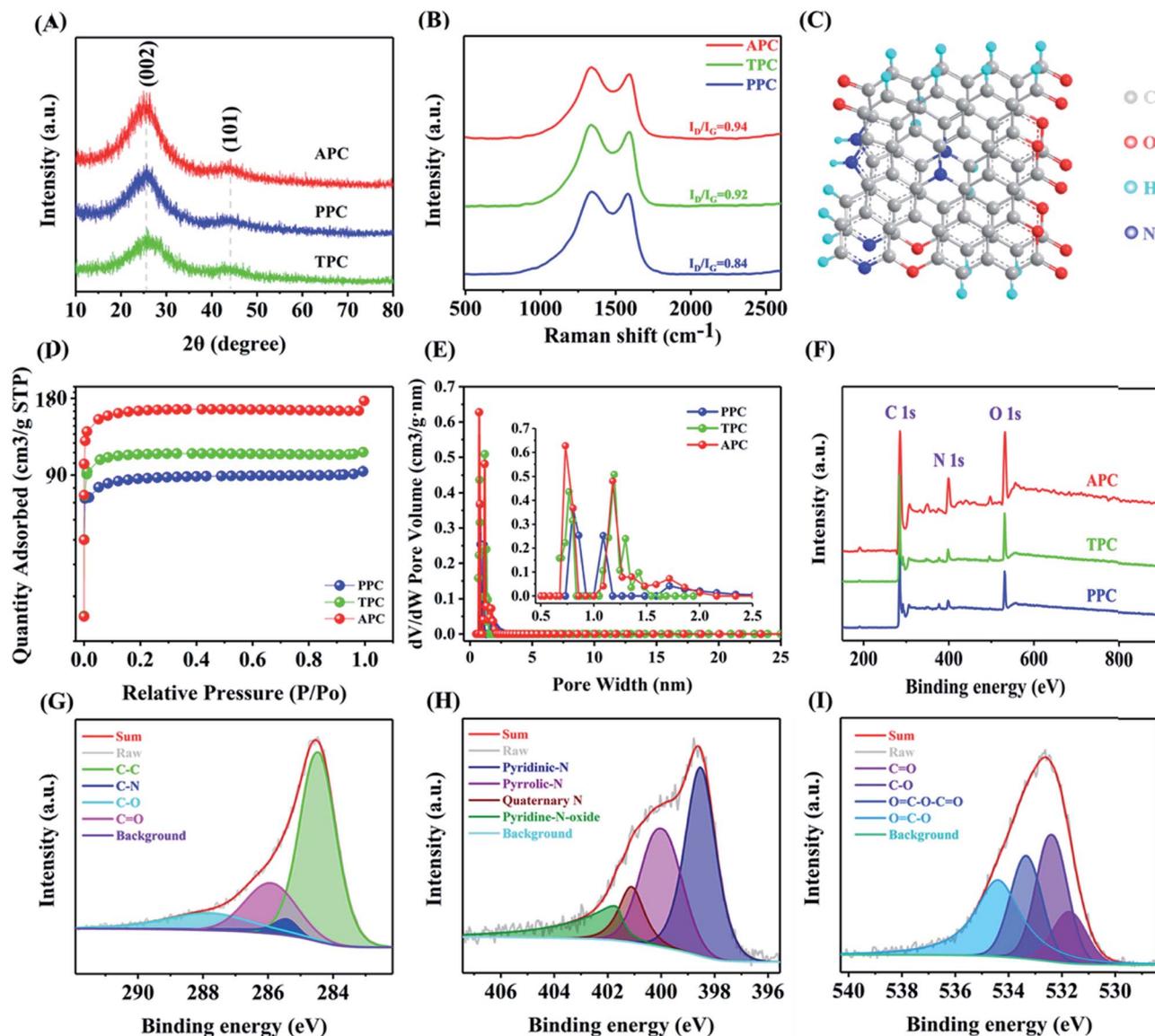
Fig. 2   (A) XRD patterns of APC, PPC, and TPC. (B) Raman spectra of APC, TPC, and PPC. (C) Molecular model of APC. (D) N_2 adsorption/desorption isotherms of PPC, TPC, and APC. (E) Pore size distribution of PPC, TPC, and APC. (F) XPS survey spectra of APC, TPC, and PPC high-resolution spectrum of APC, TPC, and PPC. (G) C 1s, (H) N 1s, and (I) O 1s spectra of APC.

energy density of 20.4 W h kg^{-1}, and a power density of 449 W K g^{-1}, as well as good cycle stability (103.2% retention after 10 000 cycles, in 1 M Na_2SO_4 aqueous electrolyte).

2.   Results and discussion

Scanning electron microscopy (SEM) and high-resolution transmission electron microscopy (HRTEM) were employed to further study the morphology of APC. As seen in SEM images in Fig. 1A–C, APC is a 3D porous structure with multiple voids and rough surfaces, which can facilitate the NH_3 activation process. In addition, macropores and mesopores in carbons emerge from the phase separation between the hydrophobic carbon and water during pyrolysis. TPC and PPC (Fig. S1 and S2,†

respectively) have similar shapes, which not only offer channels for good electrolyte contact, but also speed up the charge transfer by reducing diffusion paths.[54] The presence of micropores (Fig. 1D) was also confirmed by HRTEM. Additionally, the conductive (yellow dotted line region) and unevenly shaped layered edges (blue dotted line area) also confirm the three-dimensional porous structure. The (002) and (101) crystal planes of carbon were assigned to two separate diffraction rings in the selected-area electron diffraction pattern, respectively. The elemental mapping pictures (Fig. 1G) demonstrate that C, O, and N were uniformly dispersed on APC, further confirming the doping of N atoms.

X-ray diffraction spectroscopy was used to investigate the crystal structure of the samples (Fig. 2A). The (002) and (101)

carbon planes correspond to the peaks at 24° and 44°. The intensity of the peak ascribed to the (002) plane is weaker than that for PPC and TPC due to the existence of bigger pores and less graphitization. The XRD data show that during the chemical activation process, nano-graphitic structures emerged, which is consistent with HR-TEM results. The structural characteristics were investigated using Raman spectroscopy. As shown in Fig. 2B, the D peak and G peak can be observed, corresponding to the structural defects in the graphitic structure and the in-plane vibration of the graphitic lattice. After high temperature pyrolysis, the I_D/I_G value increased from 0.84 to 0.94, revealing the existence of more defects and disordered structures in PC materials. This phenomenon is attributed to the decrease in the average size of sp^2 domains and the introduction of abundant nitrogen functional groups during the unzipping process.[55,56] After low-temperature reduction, the I_D/I_G value decreased to 0.92 for TPC due to the removal of unstable nitrogen functional groups. Based on the above-mentioned results, we proposed the molecular model of APC, as shown in Fig. 2C. It is anticipated that this self-supporting electrode material with a distinctive 3D structure would exhibit noticeably improved electrochemical characteristics when used in aqueous SCs.

Subsequently, N$_2$ adsorption measurements were performed to further explore the pore structure of the samples. The Barrett–Emmett–Teller (BET) method was used to determine the surface area and the Barrett–Joyner–Halenda (BJH) approach for the pore size distribution, as shown in Fig. 2D and E and Table 1S.† Type I adsorption–desorption isotherms

were observed for PPC (Fig. S3†) and TPC (Fig. S4†) samples. Alternatively, the adsorption–desorption isotherms of the APC (Fig. S5†) material display a combination of type I and type IV isotherm characteristics, suggesting the creation of microporous and mesoporous structures, respectively. APC has a specific surface area of 513.33 m^2 g^{-1}, which is higher than that of PPC (278.23 m^2 g^{-1}) and TPC (342.07 m^2 g^{-1}), owing to their structural differences. Moreover, the specific surface area without NH$_3$ treatment was only 216 m^2 g^{-1} (Fig. S7† and Table 1S†). In the production of carbon compounds, NH$_3$ is considered an effective porogen. The pore size distribution of APC is narrow, with the major pore size in the range of 0.5 to 2.1 nm. The abundant micropores were beneficial for the quick transport and interpenetration of electrolyte ions, reduced ion diffusion resistance, and increased area of the material.[57,58]

The chemical composition and binding state of APC were investigated using X-ray photoelectron spectroscopy (Fig. 2F–I). The distinct peaks at 286 eV, 401 eV, and 533 eV, as shown in Fig. 2F, are ascribed to C 1s, N 1s, and O 1s, respectively. The contents of each element in the samples are summarized in Table 2S.† The high-resolution C 1s (Fig. 2G) spectra of APC exhibit peaks corresponding to C–C (285.46 eV), C–N (285.44 eV), C=O (287.10 eV), and C–O (288.01 eV), while four peaks corresponding to N-6 (398.54 eV), N-5 (400.03 eV), N–O (401.79 eV), and N–Q (401.14 eV) appeared in the high-resolution N1s spectrum (Fig. 2H). Through redox processes, N-6 (pyridine-N) and N-5 (pyrrole-N) can not only offer function groups but also boost the conductivity and wettability of carbon materials.

Fig. 3 Mechanism of agar pyrolysis.

Pyrrole nitrogen appears as a π–π* shake-up satellite peak. The O 1s spectrum (Fig. 2I) could be fitted into four peaks centered at C=O (531.67 eV), C–O (532.42 eV), O=C–O–C=O (533.37 eV), and O=C–O (534.43 eV). Thus, based on these findings, it can be concluded that the as-prepared APC has a large specific surface area and hierarchical porous carbon, which can greatly boost the performance of supercapacitors (TPC and PPC, as shown in Fig. S8 and S9,† respectively).

The schematic illustration of the carbonization mechanism of agar (Fig. 3) is based on aforementioned characterization, where numerous agar molecules undergo a cross-linking process when the temperature increases and ammonia gas is introduced, removing water molecules and some of the hydroxyl groups and ammonia gas.[59] Subsequently, the ammonia reaction takes place. As the temperature increases, the broken long-chain free radicals agglomerate. Finally, a conductive graphene

compound containing nitrogen is created. APCs have a high specific capacitance and outstanding electrochemical cycling performance because of their unique pore structure, numerous pseudocapacitive active species, and good electron/ion transport characteristics.[60–63]

To assess the supercapacitor performance of the produced agar porous carbon materials, equivalent electrochemical measurements were performed in a 6 M KOH solution. APC has bigger cyclic voltammetry (CV) curve regions than those of PPC and TPC, suggesting a higher specific capacitance, as illustrated in Fig. 4A.[38–40] The pseudocapacitance of electrode materials is obtained from the reversible oxidation–reduction reaction of nitrogen and oxygen functional groups on their surface. The reaction equation can be expressed as follows:
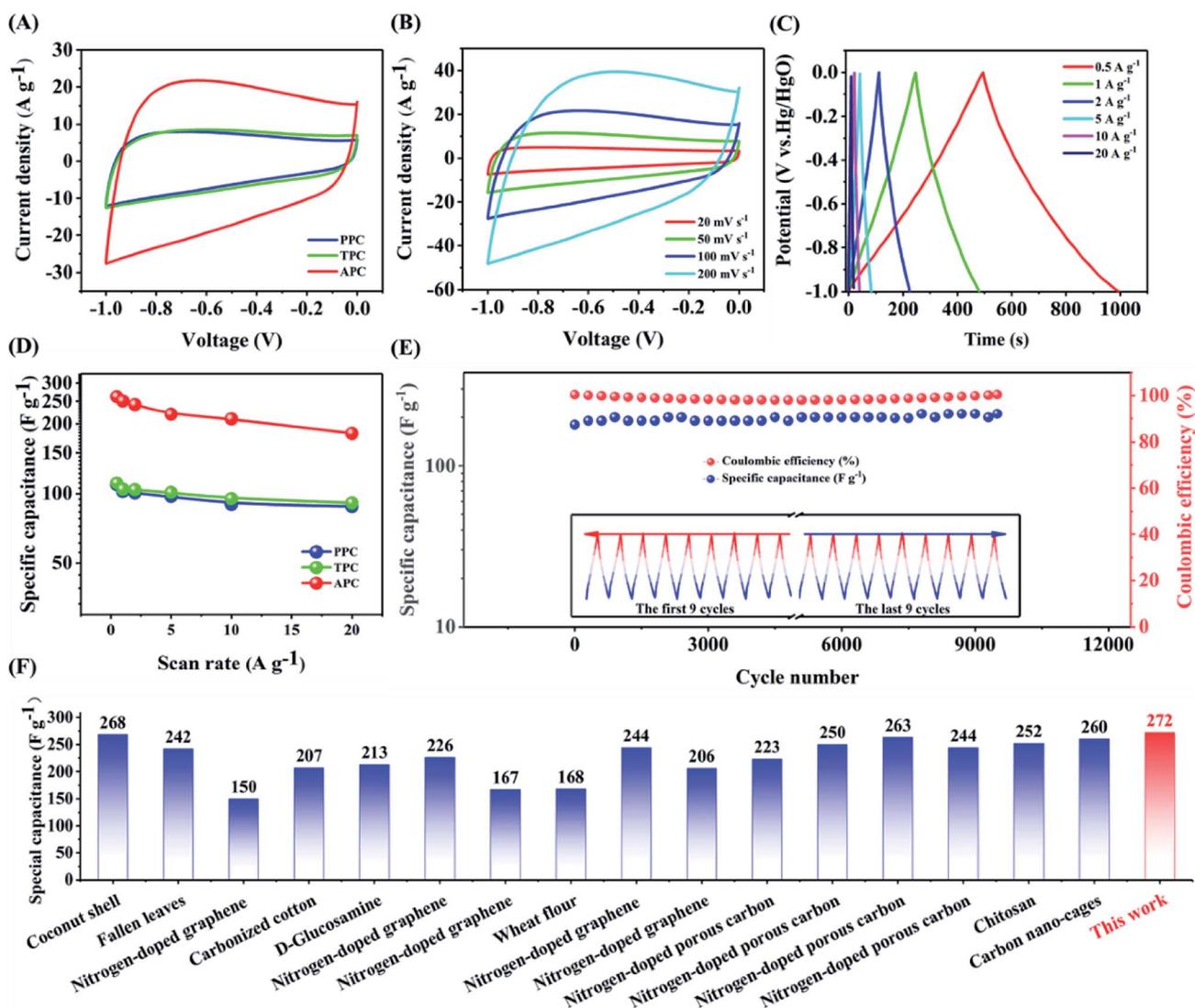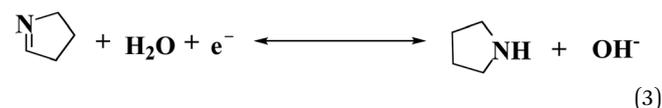

Fig. 4 (A) CV curves of PPC, TPC and APC electrodes at a scan rate of 100 mV s^{-1}. (B) CV curves of APC at different scan rates of 20, 50, 100, and 200 mV s^{-1} in 6.0 M KOH aqueous solution. (C) Galvanostatic charge/discharge curves of APC at various current densities. (D) Specific capacitances of PPC, TPC, and APC at different current densities. (E) Electrochemical stability of APC for 10 000 cycles tested at 200 mV s^{-1}. (F) Comparison of the specific capacitance of APC with that of other sugars (Table 4S†).

$$\text{(benzoquinone)} + H_2O + e^- \longleftrightarrow \text{(phenol)} + OH^- \quad (1)$$

$$\text{(pyridine)} + H_2O + e^- \longleftrightarrow \text{(NH)} + OH^- \quad (2)$$

$$\text{(pyrrole)} + H_2O + e^- \longleftrightarrow \text{(NH)} + OH^- \quad (3)$$

Furthermore, the CV curve of APC exhibits a rectangle-like form at 100 mV s^{-1} (Fig. 4B), demonstrating its strong rate

capacity. The galvanized charge–discharge curves of APC exhibit a somewhat distorted triangular form (Fig. 4C), showing that capacitance is a combination of electric double-layer and pseudocapacitance. The specific capacitance of APC, which was derived from the constant-current discharge curve (Fig. 4D) is 272 F g^{-1} at 0.5 A g^{-1} and much greater than that of PPC (216 F g^{-1}) and TPC (219 F g^{-1}). The APC electrode provided a specific capacitance of 196 F g^{-1} even at 20 A g^{-1}. Furthermore, compared to other samples with varying precursor to KOH ratios (Fig. S10 and S11†) and other previously reported porous carbon composites, APC has a greater specific capacitance (Fig. 4F and Table 4S†). The equivalent series resistance of APC (0.64 Ω) is lower than that of TPC (0.65 Ω) and PPC (0.67 Ω), showing superior conductivity, according to the Nyquist diagram (Fig. S12†). Furthermore, the surface charge transfer resistance of the APC electrode is lower than that of other samples and its charge transfer speed is quicker. Galvanostatic charge/discharge (GCD) measurements at 25 A g^{-1} were also
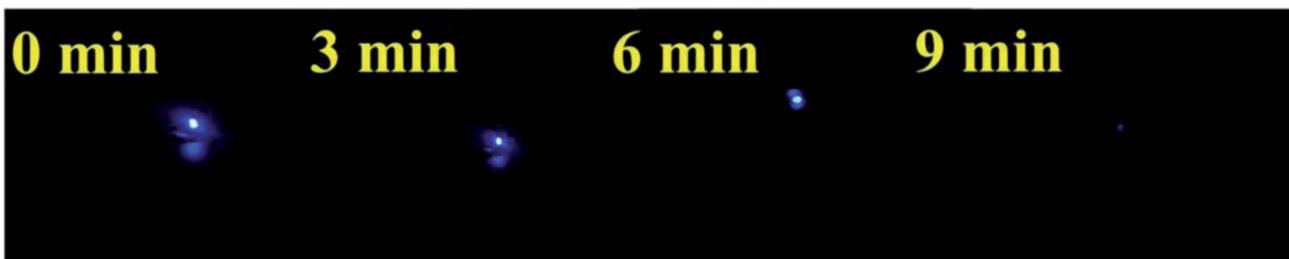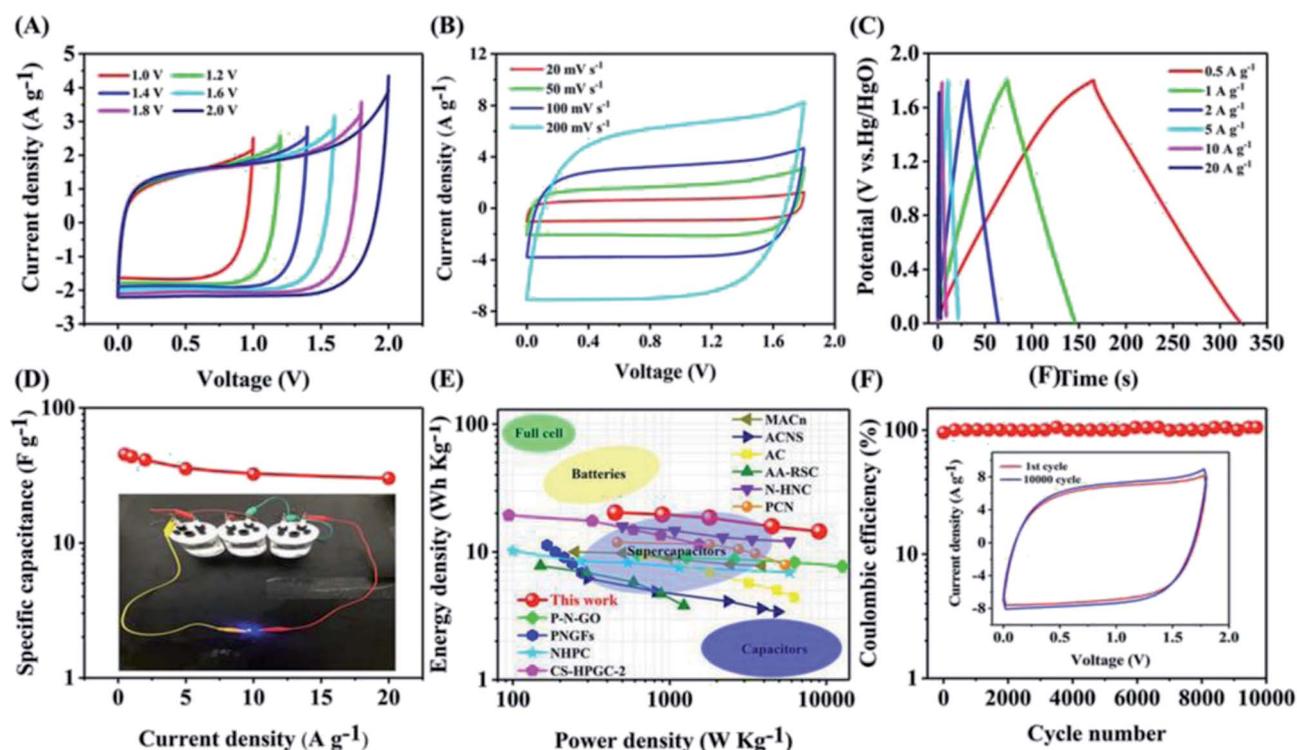

Fig. 5 (A) CV curves of the APC//APC symmetrical supercapacitor at different operation voltages at the scan rate of 50 mV s^{-1}. (B) GCD curves of the APC//APC symmetric supercapacitor at various current densities. (C) CV curves of the APC//APC symmetrical supercapacitor at different scan rates in the voltage window of 0–1.8 V. (D) Specific capacitance of the APC symmetric supercapacitor at various scan rates. (E) Ragone plot of the APC symmetric supercapacitor.[44–53] (F) Electrochemical stability of the APC symmetric supercapacitor in the 10 000 cycle test.

performed to assess the cycle stability of APC (Fig. 4E). After 10 000 cycles, the specific capacity of APC retained 98.5% of its initial capacity, demonstrating exceptional electrochemical stability.

Two-electrode symmetric supercapacitors were built and tested in 1 M Na_2SO_4 aqueous solution to further highlight the superior electrochemical capability of APC electrodes.[41–43] The CV curves of the APC//APC symmetric supercapacitors were recorded in different voltage windows at 50 mV s^{-1}, as shown in Fig. 5A. Even at 1.8 V, the anode current did not significantly increase, demonstrating that this superstar may be cycled reversibly within a voltage window of 0–1.8 V. The symmetric superstar galvanized charge–discharge curves exhibit a slightly distorted triangular form (Fig. 5B). Moreover, the CV curves of APC//APC symmetric supercapacitors were further explored at various scan rates (Fig. 5C). The CV curve was rectangular even at 200 mV s^{-1}, showing an excellent rate capability. At 2 mV s^{-1}, the APC//APC symmetric supercapacitor exhibited a specific capacity of 49.6 F g^{-1}. The specific capacitance of the symmetric superstar was also determined, as shown in Fig. 5D. Fig. 5E also shows the Ragone plot of the APC//APC symmetric superstar, which achieved a high energy density of 20.4 W h kg^{-1} and a power energy of 449 W K g^{-1}, exceeding that of nearly all previously reported carbon-based symmetric supercapacitors (Table 3S†). After 10 000 cycles, the APC//APC symmetric supercapacitor retained 103% of its initial capacity (Fig. 5F), demonstrating its good electrochemical stability. The holes in the APC material conductive paste enlarged as it became worn (Fig. S13†), allowing electrolyte ions to enter the graphene layer and store more charges. It is worth noting that three APC//APC symmetrical supercapacitor devices linked in series could light up blue commercial light-emitting diodes (LEDs), demonstrating that these electrodes have a real application value.

3. Conclusion

In conclusion, utilizing agar as a raw material, one-step carbonization produced a multilayer porous carbon material with narrow pore size distribution and co-doped nitrogen and oxygen. The electrode material possessed micropores, layered structure, and rich nitrogen–oxygen functional groups, which exhibit an outstanding specific capacitance, good rate characteristics, and ultra-long electrochemical stability. The created symmetric supercapacitors also exhibited high energy density and good electrochemical stability. At a current density of 0.5 A g^{-1}, the ultra-high specific capacity of 272 F g^{-1} was achieved. At the current density of 10 A g^{-1}, a capacity of 210 F g^{-1} was retained even in 6 M KOH electrolyte, outperforming almost all reported carbon-based supercapacitors. Moreover, after 10 000 cycles, 98.5% capacity was retained. Furthermore, the symmetric APC//APC superstar had a wide voltage window of 1.8 V, high energy density of 20.4 W h kg^{-1} and power density of 449 W Kg^{-1}, and good cycling stability (103.2% retention rate for 10 000 cycles in 1 M Na_2SO_4 aqueous electrolyte). Thus, we presented a new and cost-effective method for the synthesis of hierarchical porous carbon composites with abundant low-cost polysaccharides for improved energy storage.

Conflicts of interest

The authors declare no competing financial interests.

Acknowledgements

References

1 G. Wang, Z. Lu, Y. Li, L. Li, H. Ji, A. Feteira, D. Zhou, D. Wang, S. Zhang and I. M. Reaney, *Chem. Rev.*, 2021, **121**(10), 6124–6172.

2 H. Peng, B. Yao, X. Wei, T. Liu, T. Kou, P. Xiao, Y. Zhang and Y. Li, *Adv. Energy Mater.*, 2019, **9**(19), 1803665.

3 B. Kang and G. Ceder, *Nature*, 2009, **458**(7235), 190–193.

4 M. Salanne, B. Rotenberg, K. Naoi, K. Kaneko, P. L. Taberna, C. P. Grey, B. Dunn and P. Simon, *Nat. Energy*, 2016, **1**, 16070.

5 Z. Li, S. Gadipelli, H. Li, C. A. Howard, D. J. L. Brett, P. R. Shearing, Z. Guo, I. P. Parkin and F. Li, *Nat. Energy*, 2020, **5**(2), 160–168.

6 Y. Zhu, S. Murali, M. D. Stoller, K. J. Ganesh, W. Cai, P. J. Ferreira, A. Pirkle, R. M. Wallace, K. A. Cychosz, M. Thommes, D. Su, E. A. Stach and R. S. Ruoff, *Science*, 2011, **332**(6037), 1537–1541.

7 X. Peng, H. Liu, Q. Yin, J. Wu, P. Chen, G. Zhang, G. Liu, C. Wu and Y. Xie, *Nat. Commun.*, 2016, **7**, 11782.

8 P. Pachfule, D. Shinde, M. Majumder and Q. Xu, *Nat. Chem.*, 2016, **8**(7), 718–724.

9 K. P. Wang, L. F. Huang, N. Eedugurala, S. Zhang, M. A. Sabuj, N. Rai, X. D. Gu, J. D. Azoulay and T. N. Ng, *Adv. Energy Mater.*, 2019, **9**(47), 1902806.

10 S. Bellani, E. Petroni, A. E. Del Rio Castillo, N. Curreli, B. Martín-García, R. Oropesa-Nuñez, M. Prato and F. Bonaccorso, *Adv. Funct. Mater.*, 2019, **29**(14), 1807659.

11 A. Halder, M. Ghosh, M. A. Khayum, S. Bera, M. Addicoat, H. S. Sasmal, S. Karak, S. Kurungot and R. Banerjee, *J. Am. Chem. Soc.*, 2018, **140**(35), 10941–10945.

12 D. Zhao, C. Chen, Q. Zhang, W. Chen, S. Liu, Q. Wang, Y. Liu, J. Li and H. Yu, *Adv. Energy Mater.*, 2017, **7**(18), 1700739.

13 J. Zhou, L. Hou, S. Luan, J. Zhu, H. Gou, D. Wang and F. Gao, *Small*, 2018, **14**(36), e1801897.

14 Z. Song, L. Miao, L. Ruhlmann, Y. Lv, D. Zhu, L. Li, L. Gan and M. Liu, *Adv. Mater.*, 2021, e2104148.

15 Y. Duan, Y. Liu, Z. Chen, D. Liu, E. Yu, X. Zhang, H. Fu, J. Fu, J. Zhang and H. Du, *Green Chem.*, 2020, **22**(1), 44–53.

16 P. Li, Z. Liu, Q. Li, W. Wu and Q. Liu, *Ind. Eng. Chem. Res.*, 2014, **53**(19), 7910–7916.

17 W. Li, F. Gao, X. Wang, N. Zhang and M. Ma, *Angew. Chem., Int. Ed.*, 2016, **55**(32), 9196–9201.

18 L. Zhang, M. Cong, X. Ding, Y. Jin, F. Xu, Y. Wang, L. Chen and L. Zhang, *Angew. Chem., Int. Ed.*, 2020, **59**(27), 10888–10893.

19 A. Bakandritsos, D. D. Chronopoulos, P. Jakubec, M. Pykal, K. Čépe, T. Steriotis, S. Kalytchuk, M. Petr, R. Zbořil and M. Otyepka, *Adv. Funct. Mater.*, 2018, **28**(29), 1801111.

20 C. Choi, H. J. Sim, G. M. Spinks, X. Lepró, R. H. Baughman and S. J. Kim, *Adv. Energy Mater.*, 2016, **6**(5), 1502119.

21 H. Jin, J. Li, Y. Yuan, J. Wang, J. Lu and S. Wang, *Adv. Energy Mater.*, 2018, **8**(23), 1801007.

22 J. Cao, T. Huang, R. Liu, X. Xi and D. Wu, *Electrochim. Acta*, 2017, **230**, 265–270.

23 G. Li, S. Wang, J. Zeng and J. Yu, *Carbon*, 2021, **171**, 111–118.

24 L. Li, Q. Zhong, N. D. Kim, G. Ruan, Y. Yang, C. Gao, H. Fei, Y. Li, Y. Ji and J. M. Tour, *Carbon*, 2016, **105**, 260–267.

25 W. Liu, J. Mei, G. Liu, Q. Kou, T. Yi and S. Xiao, *ACS Sustainable Chem. Eng.*, 2018, **6**(9), 11595–11605.

26 H. Lu, S. Liu, Y. Zhang, Y. Huang, C. Zhang and T. Liu, *ACS Sustainable Chem. Eng.*, 2019, **7**(5), 5240–5248.

27 X. Wang, Y. Ding, H. Lu, F. Chen, N. Zhang and M. Ma, *Chem. Eng. J.*, 2018, **347**, 754–762.

28 J. Wei, L. Zhong, H. Xia, Z. Lv, C. Diao, W. Zhang, X. Li, Y. Du, S. Xi, M. Salanne, X. Chen and S. Li, *Adv. Mater.*, 2021, e2107439.

29 J. Lei, J. Zhou, J. Li, J. Wen, L. Su, T. Duan and W. Zhu, *Electrochim. Acta*, 2018, **285**, 292–300.

30 Z. Shang, X. An, H. Zhang, M. Shen, F. Baker, Y. Liu, L. Liu, J. Yang, H. Cao, Q. Xu, H. Liu and Y. Ni, *Carbon*, 2020, **161**, 62–70.

31 Y. Wen, T. E. Rufford, X. Chen, N. Li, M. Lyu, L. Dai and L. Wang, *Nano Energy*, 2017, **38**, 368–376.

32 X. Wu, L. Jiang, C. Long and Z. Fan, *Nano Energy*, 2015, **13**, 527–536.

33 S. Yu, N. Sun, L. Hu, L. Wang, Q. Zhu, Y. Guan and B. Xu, *J. Power Sources*, 2018, **405**, 132–141.

34 X. Feng, Y. Bai, L. Zheng, M. Liu, Y. Li, R. Zhao, Y. Li and C. Wu, *ACS Appl. Mater. Interfaces*, 2021, **13**(47), 56285–56295.

35 D. Guo, B. Ding, X. Hu, Y. Wang, F. Han and X. Wu, *ACS Sustainable Chem. Eng.*, 2018, **6**(9), 11441–11449.

36 Y. Wang, R. Liu, Y. Tian, Z. Sun, Z. Huang, X. Wu and B. Li, *Chem. Eng. J.*, 2020, **384**.

37 X. Wei, S. Wan and S. Gao, *Nano Energy*, 2016, **28**, 206–215.

38 J. Du, A. Chen, Y. Zhang, S. Zong, H. Wu and L. Liu, *J. Mater. Sci. Technol.*, 2020, **58**, 197–204.

39 P. Hu, D. Meng, G. Ren, R. Yan and X. Peng, *Appl. Mater. Today*, 2016, **5**, 1–8.

40 X.-Q. Lin, W.-D. Wang, Q.-F. Lü, Y.-Q. Jin, Q. Lin and R. Liu, *J. Mater. Sci. Technol.*, 2017, **33**(11), 1339–1345.

41 T. Liu, T. Kou, D. Bulmahn, C. Ortuno-Quintana, G. Liu, J. Q. Lu and Y. Li, *ACS Appl. Energy Mater.*, 2018, **1**(9), 5043–5053.

42 P. Wang, J. Xu, F. Xu, W. Zhao, P. Sun, Z. Zhang, M. Qian and F. Huang, *Carbon*, 2018, **134**, 391–397.

43 X. Deng, B. Zhao, L. Zhu and Z. Shao, *Carbon*, 2015, **93**, 48–58.

44 R. Zeng, X. Tang, B. Huang, K. Yuan and Y. Chen, *ChemElectroChem*, 2018, **5**(3), 515–522.

45 N. Sudhan, K. Subramani, M. Karnan, N. Ilayaraja and M. Sathish, *Energy Fuels*, 2016, **31**(1), 977–985.

46 C. Shen, R. Li, L. Yan, Y. Shi, H. Guo, J. Zhang, Y. Lin, Z. Zhang, Y. Gong and L. Niu, *Appl. Surf. Sci.*, 2018, **455**, 841–848.

47 F. R. Maria Sundar Raj, N. V. Jaya, G. Boopathi, D. Kalpana and A. Pandurangan, *Mater. Chem. Phys.*, 2020, **240**, 122151.

48 J. Li, K. Han, D. Wang, Z. Teng, Y. Cao, J. Qi, M. Li and M. Wang, *Carbon*, 2020, **164**, 42–50.

49 F. Han, D. Duan, W. Jing, Q. Wu, B. Tian, Z. Zhang, J. Liu, Y. Sun and Z. Jiang, *Ceram. Int.*, 2022, **48**(2), 2058–2067.

50 L. Guan, L. Pan, T. Peng, C. Gao, W. Zhao, Z. Yang, H. Hu and M. Wu, *ACS Sustainable Chem. Eng.*, 2019, **7**(9), 8405–8412.

51 Y. Gong, D. Li, Q. Fu, Y. Zhang and C. Pan, *ACS Appl. Energy Mater.*, 2020, **3**(2), 1585–1592.

52 G. Ghanashyam and H. K. Jeong, *J. Energy Storage*, 2019, **26**, 100923.

53 D. Dong, Y. Zhang, Y. Xiao, T. Wang, J. Wang, C. E. Romero and W. P. Pan, *J. Colloid Interface Sci.*, 2020, **580**, 77–87.

54 M. Zhang, J. Cheng, L. Zhang, Y. Li, M. Chen, Y. Chen and Z. Shen, *ACS Sustainable Chem. Eng.*, 2020, **8**, 3637–3643.

55 E. Armelin, M. M. Pérez-Madrigal, C. Alemán and D. D. Díaz, *J. Mater. Chem. A*, 2016, **4**, 8952–8968.

56 W. G. Moon, G. P. Kim, M. Lee, H. D. Song and J. Yi, *ACS Appl. Mater. Interfaces*, 2015, 7, 3503–3511.

57 D. Wang, Y. Xiao, X. Luo, Z. Wu, Y.-J. Wang and B. Fang, *ACS Sustainable Chem. Eng.*, 2017, **5**, 2509–2515.

58 B. Fang, A. Bonakdarpour, M.-S. Kim, J. H. Kim, D. P. Wilkinson and J.-S. Yu, *Microporous Mesoporous Mater.*, 2013, **182**, 1–7.

59 B. Fang, Y. Z. Wei, K. Suzuki and M. Kumagai, *Electrochim. Acta*, 2005, **50**, 3616–3621.

60 D. Guo, B. Ding, X. Hu, Y. Wang, F. Han and X. Wu, *ACS Sustainable Chem. Eng.*, 2018, **6**, 11441–11449.

61 L. Wang, T. Wei, L. Sheng, L. Jiang, X. Wu, Q. Zhou, B. Yuan, J. Yue, Z. Liu and Z. Fan, *Nano Energy*, 2016, **30**, 84–92.

62 Y. Wang, Z. Zhao, W. Song, Z. Wang and X. Wu, *J. Mater. Sci.*, 2018, **54**, 4917–4927.

63 X. Wu, D. Yang, C. Wang, Y. Jiang, T. Wei and Z. Fan, *Carbon*, 2015, **92**, 26–30.